Quantification of Turbulent Driving Forces for the Geodesic Acoustic Mode in the JFT-2M Tokamak

T. Kobayashi,[1] M. Sasaki,[2,3] T. Ido,[1] K. Kamiya,[4] Y. Miura,[5] Y. Nagashima,[2,3] K. Ida,[1,3] S. Inagaki,[2,3] A. Fujisawa,[2,3] S.-I. Itoh,[2,3] and K. Itoh[6,1,3]

[1]*National Institute for Fusion Science, National Institutes of Natural Sciences, Toki 509-5292, Japan*
[2]*Research Institute for Applied Mechanics, Kyushu University, Kasuga 816-8580, Japan*
[3]*Research Center for Plasma Turbulence, Kyushu University, Kasuga 816-8580, Japan*
[4]*National Institutes for Quantum and Radiological Science and Technology, Naka 311-0193, Japan*
[5]*Japan Atomic Energy Agency, Naka 311-0193, Japan*
[6]*Institute of Science and Technology Research, Chubu University, Kasugai 487-8501, Japan*

(Received 6 October 2017; revised manuscript received 29 November 2017; published 26 January 2018)

We investigate spatial structures of turbulence and turbulent transport modulated by the geodesic acoustic mode (GAM), from which the excitation mechanism of the GAM is discussed. The GAM is found to be predominantly excited through a localized Reynolds stress force, rather than the dynamic shearing force. The evaluated growth rate is larger than the linear damping coefficients and is on the same order of magnitude as the effective growth rate evaluated from time evolution in the GAM kinetic energy.

DOI: 10.1103/PhysRevLett.120.045002

Zonal flows in nature have attracted interest because of their great impact on the dynamics of the system [1]. Examples are seen in atmospheric circulation, solar dynamics, and magnetically confined fusion plasmas. Zonal flows in fusion plasmas are categorized into two branches, low frequency zonal flows (LFZFs) [2] and geodesic acoustic modes (GAMs) [3–18]. Both zonal flows are believed to have a beneficial property for fusion plasma confinement, that is, a turbulence transport regulation [10]. Therefore, they have been intensely studied over the last two decades. Common features of the GAMs identified in tokamaks are the acoustic scaling of the GAM frequency, toroidally and poloidally symmetric potential structure, radial propagation, coupling with density perturbation, and others. In particular, the existence of a nonlinear interaction between the GAM and turbulence has been demonstrated in many devices [3–12]. However, detailed experimental investigations focusing on the excitation mechanism have not been performed. Two different turbulent driving mechanisms have been proposed by theoreticians; those are the Reynolds stress [1] and the dynamic shearing [13,14]. To date, no experimental quantification has succeeded for these two driving forces. In order to evaluate these driving forces, a detailed measurement of the turbulent potential fluctuation with a high spatial resolution must be performed, which is still challenging. Determination of the GAM excitation mechanism is highly desirable to deepen the understanding of the turbulence structure formation that involves a nonlinear interaction between the flow and turbulence.

In this Letter, we investigate the spatial structures of turbulence and turbulent transport modulated by the geodesic acoustic mode, based on a data set obtained with the heavy ion beam probe (HIBP) [6,7]. Focusing on the energy exchange channels between the GAM and turbulence, the Reynolds stress force [1] and the dynamic shearing force [13,14] are quantified for the first time. A localized energy input into the GAM through the Reynolds stress force is found 3 cm inside the last closed flux surface, approximately a normalized minor radius of 0.9. This location corresponds to the amplitude peak of the GAM, but the characteristic scale of the energy input is much smaller than that of the eigenstructure. The dynamic shearing force is less dominant compared to the Reynolds stress force. The magnitude of the energy input into the GAM is considered to be sufficiently large to dominate linear damping terms.

JFT-2M is a medium size tokamak with a major radius R of 1.3 m and an averaged minor radius a of 0.3 m. The codirected neutral beam injection (NBI) is the main auxiliary heating for the target plasma having the line averaged electron density of 1.1×10^{19} m^{-3} in the L mode. The power of the NBI is 750 kW, which corresponds to the threshold power for achieving the L-H transition. An upper single-null divertor configuration (∇B drift directed toward the X point) is employed with the toroidal magnetic field B_t of 1.17 T, the plasma current I_p of 190 kA, and the safety factor at the flux surface enclosing 95% of the total poloidal flux q_{95} of 2.9.

A schematic of the HIBP on JFT-2M [6,7] is shown in Fig. 1(a). A singly ionized thallium beam is injected from the top side, which is charged doubly inside the plasma. From the beam energy and the beam current, the local electrostatic potential ϕ and local electron density n are determined with a sampling time of 1 μs. Four sample

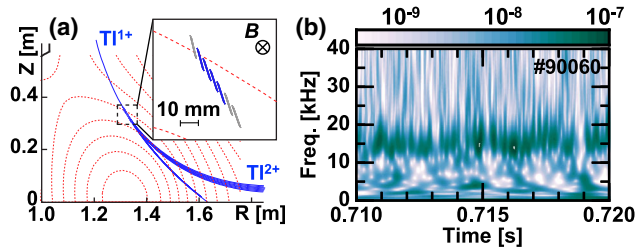

FIG. 1. (a) Schematic of the heavy ion beam probe and (b) time evolution of the potential fluctuation spectrum at $r - a \sim -3$ cm.

volumes radially and poloidally separated are simultaneously diagnosed. The angle between the row of the sample volumes and the normal vector of the magnetic surface can be altered by changing the operating parameters of the HIBP, from which the poloidal and radial spatial structures of the fluctuations can be obtained. The peripheral region ($-5 < r - a < 0$ cm) of the top side of the torus is covered in a shot-to-shot manner.

The GAM oscillation is also detected by an in-vessel magnetic probe signal at a fixed location. The radial structure of the GAM is reconstructed with respect to the magnetic fluctuation signal, which has a very good reproducibility (less than a 5% difference in mean amplitude). Moreover, in order to improve the signal to noise ratio, we perform a conditional averaging of the HIBP signals as a function of a relative time τ. This is defined as $N^{-1}\sum_{i=1}^{N}\Psi(t_i+\tau)$ for an arbitrary variable Ψ, where t_i indicates the ith time at which the phase of the GAM in the magnetic fluctuation passes zero and N is the total number of the zero passings. The use of the conditional averaging is essential to evaluate modulation patterns in the nonlinear terms, such as the Reynolds stress or the turbulent particle flux. Note that analysis methods based on Fourier decomposition were used to investigate the energy exchange between flows and turbulence [12,19] or the energy cascade among turbulence fluctuations that is stimulated by the GAM [8]. In this study we use the conditional averaging in order to treat quantities in the time domain following the theoretical expressions [13,14].

The GAM is observed in the beginning of the L-mode phase for ~200–300 ms, after which the limit-cycle oscillation emerges and the GAM oscillation is strongly damped. A typical time evolution of the electrostatic potential fluctuation spectrum from 10 ms after the NBI turn-on is shown in Fig. 1(b). A preceding study revealed basic properties of the GAM, including the $m = 0$ poloidal structure of the potential oscillation, the radial eigenmode structure, the modulation of the ambient turbulence and turbulent transport, and others [6,7]. Figure 2(a) shows the radial profile of the frequency dependent potential power spectrum during the L mode. The black dots show a theoretical prediction of the GAM frequency c_s/R, where c_s shows the sound speed. A coherent spectral peak of the GAM appears at $f_{\mathrm{GAM}} = 15$ kHz with a spectral width of

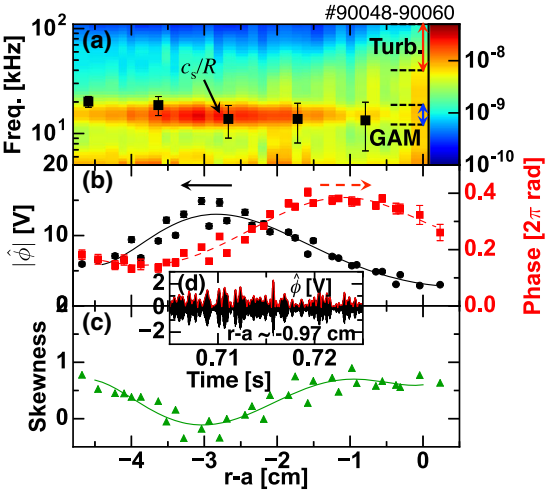

FIG. 2. Radial profiles of (a) the frequency dependent potential power spectrum density, (b) the GAM amplitude and phase, (c) the skewness of GAM amplitude, and (d) the time evolution of the GAM potential fluctuation and its envelope at $r - a \sim -1$ cm.

$\delta f_{\mathrm{GAM}} \sim 5$ kHz. Although c_s/R varies with the radius, the GAM frequency remains almost constant, being referred to as the eigenmode GAM [15]. Three quantities that have different time scales are defined: a mean quantity $\bar{\Psi}$, an oscillation quantity in the GAM frequency range $\hat{\Psi}$ ($13 \le f \le 18$ kHz), and a turbulent fluctuation $\tilde{\Psi}$ ($40 \le f \le 110$ kHz), where Ψ is an arbitrary variable. The frequency ranges for the GAM and the turbulence are shown in Fig. 2(a). Figure 2(b) shows the radial profiles of the amplitude and phase of the conditional averaged $\hat{\phi}$ signal. A peak appears at $r - a \sim -3$ cm, at which the slope of the phase is positive, showing the outward propagation of the GAM. Towards the edge, the slope of the phase is gradually flattened and reverses at $r - a \sim -1$ cm, possibly due to the reflection of the GAM at the boundary [20]. Figure 2(d) shows the time evolution of $\hat{\phi}$ and its amplitude at $r - a \sim -1$ cm. The amplitude of the GAM fluctuates in time and shows an intermittent property [4,9,11]. It is worthwhile to investigate the higher-order moments of the GAM amplitude to quantify the intermittency. Figure 2(c) shows the radial profile of the skewness, which is the third order moment of the GAM amplitude. A positive (negative) value of the skewness indicates that the data are characterized by positive (negative) spikes. Skewness is around zero at $r - a \sim -3$ cm, and increases towards the edge. The variation in the skewness profile is discussed below. Kurtosis, the fourth order moment, has a relatively large scatter of points and its behavior is not conclusive.

Modulations in the turbulence amplitude in the potential fluctuation $\hat{S}$ and the turbulence wave number $\hat{k}_r$ are induced by the GAM. Figures 3(a) and 3(b) show the amplitude and phase of $\hat{S}$ and $\hat{k}_r$ with respect to the magnetic field fluctuation in the GAM. The turbulence wave numbers derived from the potential fluctuation and

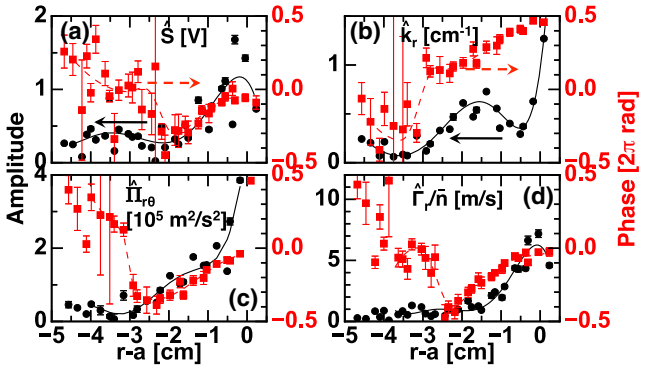

FIG. 3. Amplitude and phase profiles of the turbulence and turbulent transport modulation at the GAM frequency: (a) turbulence amplitude, (b) radial wave number, (c) Reynolds stress, and (d) particle flux. The left and right vertical axes scale amplitude and phase, respectively.

from the density fluctuation are approximately identical. For the sake of a better signal to noise ratio, the latter is used here. The Reynolds stress, i.e., the turbulent momentum flux, in the magnetized plasmas is defined as $\tilde{\Pi}_{r\theta} \equiv -\langle \tilde{E}_r \tilde{E}_\theta \rangle / B^2 \sim -\bar{k}_r \bar{k}_\theta \bar{S}^2 / 2B^2$, where $\langle \cdot \rangle$ shows a long time averaging. The Reynolds stress modulation by the GAM is evaluated as $\hat{\Pi}_{r\theta} = \bar{\Pi}_{r\theta}(\hat{k}_r/\bar{k}_r + 2\hat{S}/\bar{S})$, which is shown in Fig. 3(c). Here, the modulation in the poloidal wave number k_θ by the modulational coupling is negligibly small, as is the case in Ref. [21]. In the present case, $|\hat{k}_r|/\bar{k}_r \gg |\hat{S}|/\bar{S}$ holds. At $r - a \sim -3$ cm, there is a jump in the phase profile of $\hat{\Pi}_{r\theta}$, which produces a large divergence of the Reynolds stress, i.e., Reynolds stress force. The turbulence particle flux is defined as $\tilde{\Gamma}_r \equiv \langle \tilde{E}_\theta \tilde{n} \rangle / B \sim -i \bar{k}_\theta \langle \tilde{\phi}\, \tilde{n} \rangle / B$, where i is the imaginary unit. At the top side of the torus where the sample volumes of the HIBP are present [Fig. 1(a)], the modulation of the particle flux is expected to be maximum. Figure 3(d) shows the GAM modulation component of the turbulent particle flux normalized by the mean density $\hat{\Gamma}_r/\bar{n}$. The phase jump exists at a different location, $r - a \sim -2.5$ cm.

It should be mentioned that the LFZF is known to have an enhanced inertia, which arises from the coupling with the toroidal flow perturbation. It is estimated as $1 + 1.6q^2/\sqrt{a/R} \sim 30$ in the banana regime [22]. Therefore, the GAM is allowed to be excited by a 30 times smaller force compared with the LFZF [21].

Here, the energy exchange between the GAM and turbulence through the Reynolds stress [1] and the dynamic shearing [13,14] are discussed. The Reynolds stress force can resonantly oscillate with the $E \times B$ flow of the GAM via the modulational coupling, through which the turbulence energy is transformed into the GAM energy. Meanwhile, the GAM can also gain energy from the particle flux modulation that enhances the density perturbation of the GAM, which is called the dynamic shearing process. From the model equations [14], the rate of change in the GAM kinetic energy ($K_{\mathrm{GAM}} \equiv |\hat{V}_{E\times B}|^2$) is derived as $K_{\mathrm{GAM}}^{-1} \partial_t K_{\mathrm{GAM}} = \gamma_{\mathrm{RS}} + \gamma_{\mathrm{DS}} - \gamma_L$, where γ_{RS} and γ_{DS} account for the Reynolds stress drive and the dynamic shearing drive of the GAM, respectively. The linear damping rate is denoted as γ_L. In general, an oscillatory force $\hat{F}$ drives the GAM with a rate of $\gamma = 2|\hat{F}||\hat{V}_{E\times B}|^{-1} \cos(\theta_F - \theta_{V_{E\times B}})$, where $\theta_F - \theta_{V_{E\times B}}$ is the cross phase between $\hat{F}$ and $\hat{V}_{E\times B}$. The Reynolds stress force and the dynamics shearing force are given as $\hat{F}_{\mathrm{RS}} = -r^{-1}\partial_r r \hat{\Pi}_{r\theta}$ and $\hat{F}_{\mathrm{DS}} = ic_s^2/(4\pi^2 f_{\mathrm{GAM}} R) r^{-1} \partial_r r (\hat{\Gamma}_r/\bar{n})$, respectively. The equilibrium density gradient is expected to be weak enough in $r - a < -1.5$ cm for neglecting the $\partial_r \bar{n}$ term. For estimating the dynamic shearing force, the poloidal mode structure of the particle flux modulation is essential, but it is unknown. Here, we follow a theoretical assumption [14], in which the particle flux modulation is regarded to have the up-down asymmetry, as synchronizing the density perturbation. A finite phase difference between the particle flux modulation and the density perturbation lessens the dynamic shearing force. Therefore, the evaluation here gives the largest possible evaluation of the dynamic shearing force.

Figure 4 shows the amplitude and phase of the evaluated force, as well as the expected growth rates induced by the Reynolds stress force and the dynamic shearing force. The present evaluations are given based on the conditional averaged profiles of the amplitude and phase that correspond to the saturation phase of the GAM activity. A local maximum in $|\hat{F}_{\mathrm{RS}}|$ appears where the jump in the phase profile of $\hat{\Pi}_{r\theta}$ exists, at $r - a \sim -3$ cm. Around the peak,

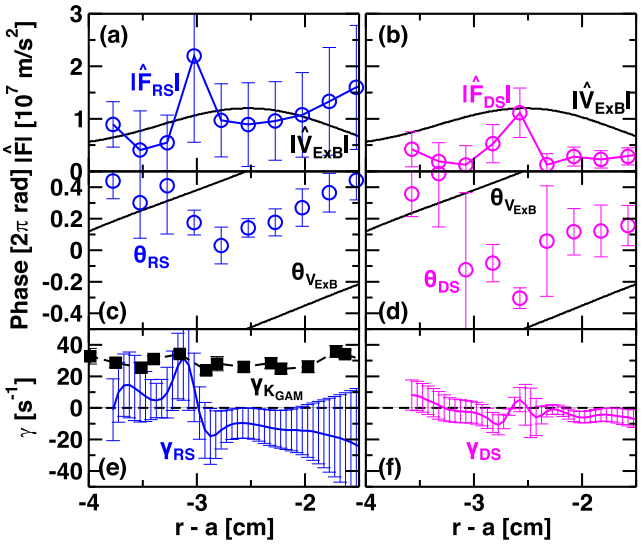

FIG. 4. Radial profiles of (a),(b) the modulation amplitude, (c), (d) the modulation phase, and (e),(f) the expected growth rate for the Reynolds stress force and dynamic shearing force, respectively. An effective growth rate evaluated from the time evolution of the GAM kinetic energy is overplotted in (e).

the phase difference between the force and the flow becomes zero. As a result, a local peak of $\gamma_{RS} \sim 3 \times 10^4$ s^{-1} emerges at $r - a \sim -3$ cm in the profile. In the outer radii of the peak, $r - a > -3$ cm, the growth rate becomes negative; i.e., a nonlinear damping of the GAM is expected. Although the energy input into the GAM is localized, the eigenmode has a wider radial structure. A similar observation, a localized energy input that excites a global LFZF, was reported in a cylindrical plasma column [23]. In contrast to γ_{RS}, γ_{DS} is insignificant in the entire peripheral region. Note again that the present value of γ_{DS} is given as the largest possible evaluation. The collisionless damping (Landau damping) rate [16] and the collisional damping rate [18] are given as $\gamma_{Landau} \sim 1 \times 10^4$ s^{-1} and $\gamma_{col} \sim 50$ s^{-1}, respectively. The linear damping rate is slightly smaller than the expected growth rate. The evaluated growth rate is therefore considered to be sufficiently large to account for the GAM growth. The nonlinear saturation mechanism of the GAM, which can be assessed based on the higher harmonics of the GAM spectrum [17], will be the subject of future study. An effective growth rate can be directly evaluated from the time evolution of the GAM kinetic energy K_{GAM}. During the time frames in which K_{GAM} increases through a threshold value, $\gamma_{K_{GAM}}$ is defined as $K_{GAM}^{-1}\partial_t K_{GAM}$. The radial profile of ensemble averaged $\gamma_{K_{GAM}}$ is overplotted in Fig. 4(e). Since the GAM has a wider eigenfunction, $\gamma_{K_{GAM}}$ shows a flat profile. Overall, the effective growth rate of $\sim 3 \times 10^4$ s^{-1} is on the same order as γ_{RS}.

The growth rate induced by the Reynolds stress force γ_{RS} in Fig. 4(e) peaks at the radius where the skewness is around zero [Fig. 2(c)]. Beyond the models describing the GAM spatial structure [15], we attempt to interpret this coincidence. At the location where the net growth rate is zero or negative, local growth of the GAM is prohibited. Therefore, a finite GAM component in these locations can be regarded as a portion spatially transmitted by forming an eigenmode structure or by a radial propagation. These portions can have a different statistical property from the locally excited component. The skewness profile implies that the local growth and decay of the GAM follow Gaussian statistics, while the spatially transmitted portion involves positive spikes. An analogy can be found in models of the blob filament dynamics in the scrape-off layer plasmas [24].

In summary, we investigated spatial structures of turbulence and turbulent transport modulated by the geodesic acoustic mode, from which nonlinear interplays between the GAM and turbulence were discussed. The GAM was found to be predominantly excited through a localized Reynolds stress force, rather than the dynamic shearing force. The magnitude of the energy input into the GAM was considered to be sufficiently large, as to dominate linear damping terms.

We thank G. D. Conway, K. Hallatschek, and G. Birkenmeier for useful discussions, and the late H. Maeda, Y. Hamada, M. Mori, Y. Kamada, S. Sakakibara, and K. Hoshino for strong support. This work is partly supported by the Grant-in-Aid for Scientific Research of Japan Society for the Promotion of Science, Japan (Grants No. 17K14898, No. 16K18335, No. 16H02442, No. 15H02155). The collaboration programs of National Institute for Quantum and Radiological Science and Technology and of Research Institute for Applied Mechanics, Kyushu University are also appreciated.

[1] P. H. Diamond, S.-I. Itoh, K. Itoh, and T. S. Hahm, Plasma Phys. Controlled Fusion **47**, R35 (2005).
[2] A. Fujisawa *et al.*, Phys. Rev. Lett. **93**, 165002 (2004).
[3] G. R. McKee *et al.*, Phys. Plasmas **10**, 1712 (2003).
[4] A. Melnikov *et al.*, Plasma Phys. Controlled Fusion **48**, S87 (2006).
[5] A. Kramer-Flecken, S. Soldatov, H. R. Koslowski, and O. Zimmermann (TEXTOR Team), Phys. Rev. Lett. **97**, 045006 (2006).
[6] T. Ido *et al.*, Plasma Phys. Controlled Fusion **48**, S41 (2006).
[7] T. Ido *et al.*, Nucl. Fusion **46**, 512 (2006).
[8] C. Holland, G. R. Tynan, R. J. Fonck, G. R. McKee, J. Candy, and R. E. Waltz, Phys. Plasmas **14**, 056112 (2007).
[9] J. Cheng, L. W. Yan, K. J. Zhao, J. Q. Dong, W. Y. Hong, J. Qian, Q. W. Yang, X. T. Ding, X. R. Duan, and Y. Liu, Nucl. Fusion **49**, 085030 (2009).
[10] G. Conway, C. Angioni, F. Ryter, P. Sauter, and J. Vicente, Phys. Rev. Lett. **106**, 065001 (2011).
[11] J. C. Hillesheim, W. A. Peebles, T. A. Carter, L. Schmitz, and T. L. Rhodes, Phys. Plasmas **19**, 022301 (2012).
[12] M. Xu *et al.*, Phys. Rev. Lett. **108**, 245001 (2012).
[13] K. Hallatschek and D. Biskamp, Phys. Rev. Lett. **86**, 1223 (2001).
[14] K. Itoh, K. Hallatschek, and S.-I. Itoh, Plasma Phys. Controlled Fusion **47**, 451 (2005).
[15] K. Itoh, S.-I. Itoh, P. H. Diamond, A. Fujisawa, M. Yagi, T. Watari, Y. Nagashima, and A. Fukuyama, Plasma Fusion Res. **1**, 037 (2006).
[16] Z. Gao, K. Itoh, H. Sanuki, and J. Dong, Phys. Plasmas **15**, 072511 (2008).
[17] M. Sasaki, K. Itoh, Y. Nagashima, A. Ejiri, and Y. Takase, Phys. Plasmas **16**, 022306 (2009).
[18] Z. Gao, Phys. Plasmas **20**, 032501 (2013).
[19] P. Manz, M. Ramisch, and U. Stroth, Phys. Rev. Lett. **103**, 165004 (2009).
[20] Y. Nagashima *et al.*, Plasma Phys. Controlled Fusion **51**, 065019 (2009).
[21] T. Kobayashi, K. Itoh, T. Ido, K. Kamiya, S. I. Itoh, Y. Miura, Y. Nagashima, A. Fujisawa, S. Inagaki, K. Ida, and K. Hoshino, Phys. Rev. Lett. **111**, 035002 (2013).
[22] K. Itoh and S.-I. Itoh, Plasma Phys. Controlled Fusion **38**, 1 (1996).
[23] Y. Nagashima *et al.*, Phys. Plasmas **16**, 020706 (2009).
[24] D. D'Ippolito, J. Myra, and S. Zweben, Phys. Plasmas **18**, 060501 (2011).